nature catalysis

Article

https://doi.org/10.1038/s41929-026-01514-x

Dynamics of a $Cu/ZnO/Al_2O_3$ catalyst revealed by operando transmission electron microscopy during CO_2 hydrogenation

Received: 16 November 2023

Accepted: 5 March 2026

Published online: 01 April 2026

Check for updates

Maxime Boniface[1] ✉, Thomas Götsch[1], Jinhu Dong[1], Jutta Kröhnert[1], Elias Frei[1], Annette Trunschke[1], Robert Schlögl[1,2], Beatriz Roldan Cuenya[3] & Thomas Lunkenbein[1,4] ✉

$Cu/ZnO/Al_2O_3$ catalysts are the industrial standard for methanol synthesis. Their high activity stems from the synergy between Cu and Zn, but their precise structure under CO_2 hydrogenation conditions remains unknown. Here we show, using operando transmission electron microscopy, that the formation of ZnO_x overlayers and CuZn surface alloys on Cu surfaces can be reversible and is mediated by the operating temperature and the chemical potential of the gas phase. Lower temperatures and more oxidative conditions lead to thicker ZnO_x overlayers. At elevated temperatures, the overlayer coverage opens, exposing Cu nanoparticle surfaces to the feed and enabling CO_2 activation. Furthermore, we show that CuZn alloys are transient species and are re-oxidized by H_2O formed during the reaction. This implies that, in CO_2 hydrogenation conditions, CuZn and Cu–ZnO surface states may coexist and continuously convert into one another as the local chemical potential oscillates throughout steady-state operation. Maintaining this fluctuation might be critical to the lifetime and performance of the catalyst.

$Cu/ZnO/Al_2O_3$ (CZA) catalysts have been used industrially since the mid-1960s for both the water–gas shift reaction and methanol synthesis from syngas. Methanol synthesis is of growing importance with a current demand around 112 million metric tonnes per year[1], and is of particular interest to valorize captured CO_2. Furthermore, methanol produced from CO_2 and H_2 is discussed to play a key role as an energy storage molecule, owing to its gravimetric energy comparable to that of ammonia[2].

Although this catalyst system has seen widespread adoption, research efforts still continue to elucidate the complete reaction mechanism. In particular, there has been considerable debate on the nature of the synergistic effect between Cu and Zn and whether active sites are Cu–Zn bimetallic or Cu–ZnO interfacial sites[3–5]. Recent evidence indicates that, although both sites are active for methanol synthesis, Cu–ZnO sites seem superior[6–8]. The key to understanding the activation, performance and deactivation of this catalyst system seems to lie in the delicate interplay between the formation of a CuZn alloy phase and the wetting of Cu nanoparticles by ZnO_x after partial reduction through the formation of strong metal–support interactions (SMSI)[9–13]. Characterization of such a complex system is challenging, as the highly dynamic nature of the CZA catalyst requires the use of operando and in situ techniques[14]. It has been shown that the ZnO_x coverage on Cu surfaces can respond to the chemical potential of the gas feed[9,15], suggesting that post-catalytic ex situ studies could lead to misleading conclusions about the true working state of the catalyst. So far, in situ and operando synchrotron-based X-ray techniques[7,8,12,16–22]

[1]Fritz-Haber-Institut der Max-Planck-Gesellschaft, Department of Inorganic Chemistry, Berlin, Germany. [2]Department of Heterogeneous Reactions, Max-Planck-Institute for Chemical Energy Conversion, Mülheim an der Ruhr, Germany. [3]Fritz-Haber-Institut der Max-Planck-Gesellschaft, Department of Interface Science, Berlin, Germany. [4]University of Bayreuth, Bavarian Center for Battery Technology (BayBatt) and Chair of Operando-Analytics for Electrochemical Energy Storage, Bayreuth, Germany. ✉e-mail: mboniface@fhi-berlin.mpg.de; lunkenbein@fhi-berlin.mpg.de

https://doi.org/10.1038/s41929-026-01514-x

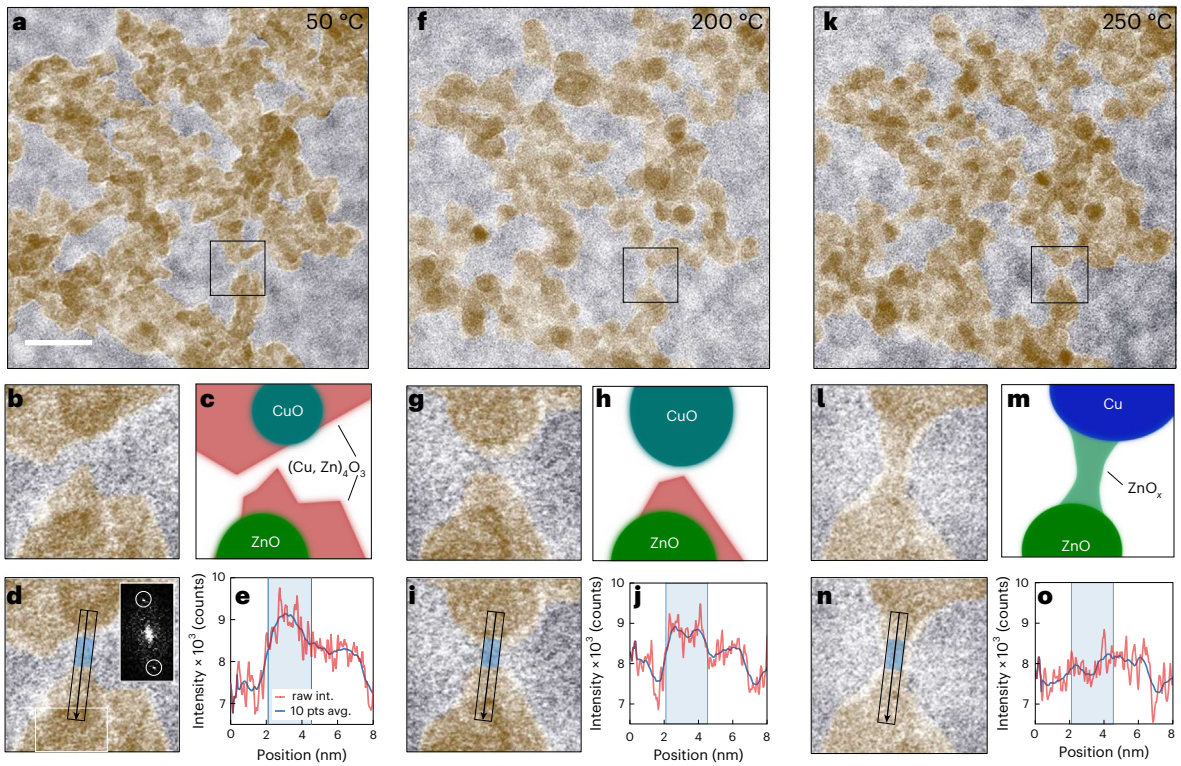

Fig. 1 | Morphological changes of the calcined CZA sample studied by operando TEM during activation in hydrogen. a–**e**, Initial precursor state. CuO and ZnO particles are embedded in a (Cu,Zn) carbonate matrix. Overview TEM image (**a**). Magnified region of the area highlighted in **a** (black box) (**b**). Schematic representation of **b** (**c**). Magnified region of the area highlighted in **a** (black box) (**d**), including a fast Fourier transform taken from the region highlighted by the white box. Intensity profile taken from the area highlighted in **d** (black box, arrow) (**e**). **f**–**j**, In a first step up to 200 °C, the carbonate matrix disappears in favour of fewer and larger oxide nanoparticles. Overview TEM image from the same region as in **a** at 200 °C (**f**). Magnified region of the area highlighted in **f** (black box) (**g**). Schematic representation of **g** (**h**). Magnified region of the area highlighted in **f** (black box) (**i**). Intensity profile taken from the area highlighted in **i** (black box, arrow) (**j**). **k**–**n**, in a second step, CuO particles reduce to Cu. Partially reduced ZnO_x becomes mobile and wets Cu surfaces, forming a bridge-like feature in the area highlighted in the inset. Overview TEM image from the same region as in **a** and **f** at 250 °C (**k**). Magnified region of the area highlighted in **k** (black box) (**l**). Schematic representation of **l** (**m**). Magnified region of the area highlighted in **k** (black box) (**n**). Intensity profile taken from the area highlighted in **n** (black box, arrow) (**o**). The flat image intensity profile shows that a feature of even thickness has appeared in the highlighted area. Images are artificially colored for representation. The original images are shown in Supplementary Fig. 3.The dose rate was 1,105 $e^- Å^{-2} s^{-1}$. Conditions: gas composition $He:H_2 = 9:1$, pressure 790 mbar, heating rate 5 K min^{-1}. Scale bar, 20 nm.

have brought the most important contributions to the field, offering crucial insights into the structure and chemistry of CZA catalysts during reduction and CO_2 hydrogenation. These techniques, however, average over many particles and can neither investigate the local morphology and structure of the catalyst nor probe the spatial distribution of the Cu, Cu oxide and ZnO phases.

Operando and in situ transmission electron microscopy (TEM) can provide such insight, and several contributions have been made[6,23–25] using established experimental workflows developed on simpler catalyst systems such as Pt nanoparticles for CO oxidation[26–29] or the SMSI of supported noble metals[30]. Recently, operando scanning (S)TEM was used to explore the SMSI state of a model Ni/TiO_2 catalyst for CO_2 hydrogenation[31]. In situ TEM has emerged over the past decade[32,33] with the advent of commercial microelectromechanical system-based nanoreactors as an invaluable tool to probe catalysts in their working environments at pressures up to 1 bar. Such systems can be paired with online mass spectrometry[34] (MS) in an operando experiment, allowing the detection of conversion and the formation of products alongside morphological insight from imaging, and structural information from selected area electron diffraction (SAED).

In this work, operando TEM was used to provide unique insight into the morphological and structural evolution of an industrially relevant CZA catalyst during reductive activation and under CO_2 hydrogenation conditions. We show that the wetting of Cu particles by ZnO_x is reversible as well as temperature and CO_2 content dependent. Under reaction conditions, the ZnO_x coverage diminishes, thereby exposing the Cu/ZnO_x perimeters and allowing CO_2 activation. The results are complemented by in situ STEM combined with electron energy loss spectroscopy (STEM–EELS) measurements and diffuse reflectance infrared Fourier transform spectroscopy (DRIFTS). Finally, we explore the reversibility of CuZn bulk alloying in CO_2/H_2 feeds and show that H_2O produced by the reverse water–gas shift (RWGS) reaction contributes to quickly re-oxidize CuZn alloys to Cu–ZnO sites. This suggests that continuous alloying and re-oxidation could be critical to the performance of this catalyst.

Results

Activation of the CZA precursor

The CZA catalyst system has previously been characterized by us using a wide variety of techniques. This is summarized in Supplementary Table 1 and has been used as a basis for this study. The state of the art on CZA catalysts for methanol synthesis was also summarized in a recent review article[35]. For the present study, an experiment was designed to investigate the morphological and structural evolution of the CZA catalyst under varying conditions, from activation to operation in methanol synthesis and RWGS-related feeds, within a pressure range of 616–790 mbar. A graphical summary of the temperature profiles and gases used can be found in Supplementary Fig. 1.

The synthesis of our CZA precursor includes a final calcination step[36]. The catalyst must first be activated in situ by reduction in diluted

https://doi.org/10.1038/s41929-026-01514-x

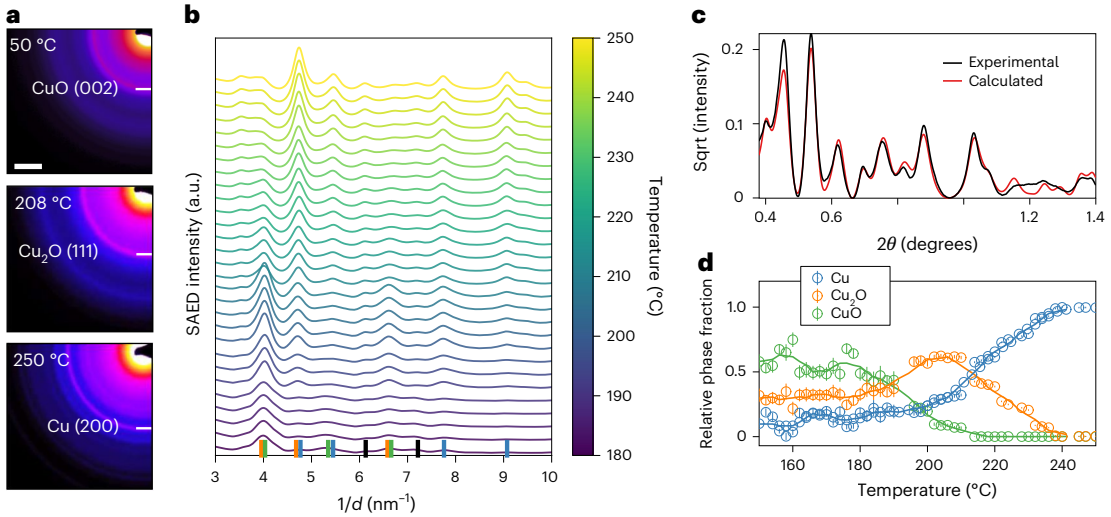

Fig. 2 | Structural changes during activation. a, Selected SAED patterns recorded at different stages of the reductive activation process. Scale bar, 2 nm^{-1}. **b**, Integrated SAED patterns after background subtraction during reductive activation. Characteristic peaks of the reduction intermediate Cu_2O appear between 196 °C and 232 °C. The Cu_2O fraction found below 196 °C is a fitting artefact due to the overlap of the CuO and Cu_2O (111) reflections. Both CuO (green lines) and Cu_2O (orange lines) reflections disappear in favour of Cu (blue lines), with reduction being complete at 250 °C. The black lines indicate reflection associated with ZnO. $1/d$ denotes the reciprocal lattice plane distance (d). **c**, An example of an experimental integrated SAED pattern at 220 °C and the matching calculated pattern from Rietveld fitting indicating the coexistence of Cu_2O and Cu. The square root (Sqrt) of the intensity is plotted. **d**, Relative weight phase fraction of Cu species calculated from Rietveld fits. The error values were calculated from the Rietveld fitting errors. Conditions: gas composition $He:H_2 = 9:1$, pressure 790 mbar, heating rate 5 K min^{-1}, electron dose rate 3.4 $e^- Å^{-2} s^{-1}$.

hydrogen, similar to industrial activation protocols. The temperature was ramped up to 250 °C at a rate of 5 K min^{-1} and the precursor left to reduce for 2 h. TEM (Fig. 1), SAED (Fig. 2) and MS (Supplementary Fig. 2) results were compared to reveal which phases were present throughout the temperature ramp. Based on these results, we identified two main reduction steps.

In its initial state, the aggregates of the precursor consist of ZnO and CuO nanoparticles (3–5 nm) embedded in an amorphous $(Cu,Zn)_4O_3CO_3$ matrix (Fig. 1a–e), as determined in previous studies[36–39]. The raw data for Fig. 1 can be found in Supplementary Fig. 3. The attribution of these three phases is challenging, as the carbonate phase is too sensitive to electron beam damage (Supplementary Fig. 4 and Supplementary Video 1) to allow direct identification by STEM–EELS or energy-dispersive X-ray spectroscopy (EDS) measurements. It cannot be directly assigned in an operando experiment. To address these challenges, we controlled for electron beam damage by limiting our working dose rate to about 1,000 $e^- Å^{-2} s^{-1}$ (Supplementary Video. 2), and relying partly on prior knowledge of the system[17,36–38] as well as on an analysis of the precursor by high-resolution TEM (Supplementary Fig. 5). This analysis shows that the spherical nanoparticle domains correspond to CuO in the precursor, while ZnO is present as shapeless, elongated domains. For this reason, we attribute the domain at the top of Fig. 1c as CuO. Moreover, the domain at the bottom of Fig. 1c can be identified as ZnO from its characteristic (100) lattice fringes at 2.81 Å. Having located CuO and ZnO domains in the area of interest, we attribute the remaining lighter-contrast phase to the $(Cu,Zn)_4O_3CO_3$ carbonate. This is supported by the fact that this phase disappears during the reductive activation process, in favour of larger CuO_x and ZnO domains. This matches the behaviour of the $(Cu,Zn)_4O_3CO_3$ phase we observed in previous work[36,38].

As the temperature increases, the H_2O partial pressure rises sharply from 100 °C onwards (Supplementary Fig. 2). This is accompanied by drastic morphological changes, as the carbonate matrix progressively disappears in favour of larger CuO and ZnO domains (Fig. 1f–j), although the acquired SAED patterns remain unchanged (Fig. 2a,b). This is because $(Cu,Zn)_4O_3CO_3$ is amorphous and thus does not contribute to diffraction[36]. Such so-called high-temperature carbonates have been shown to decompose completely during reduction[17]. This process is critical to the final morphology of the activated catalyst[40]. The onset of the reduction corresponds to a second step from about 190 °C onwards, in agreement with previous temperature-programmed reduction results[36,41]. The CuO partially reduces to Cu_2O, with CuO reflections at 5.35 nm^{-1} and 3.97 nm^{-1} fading in favour of Cu_2O peaks at 4.06 nm^{-1} and 4.67 nm^{-1}, respectively (Fig. 2a,b). The phase fractions of the Cu containing parts of the sample were determined by Rietveld fitting[42] of integrated SAED ring patterns[43] (Fig. 2c). The Cu^I reduction intermediate is transient, as characteristic Cu_2O peaks disappear entirely before 234 °C is reached (Fig. 2d). This is in excellent agreement with previous in situ X-ray diffraction (XRD)[20], extended X-ray absorption fine structure[18] and X-ray absorption near edge structure[22] reports. We leverage here the advantageous time resolution of electron diffraction, as the short lifetime of Cu_2O, here measured to be 7.2 ± 0.8 min, makes it difficult to detect with XRD. From 205 °C onwards, both Cu^{II} and Cu^I oxide species disappear progressively in favour of fully reduced metallic Cu (Fig. 2d). The Cu phase fraction shows a linear increase over the rest of the programmed temperature ramp, reaching its maximum at around 240 °C (Fig. 2d). Furthermore, a careful particle size analysis shows that nanoparticles sinter during this second activation step, with the particle size distribution average rising from 4 nm of CuO for the precursor to 7.5 nm of Cu after 2 h at 250 °C (Supplementary Fig. 6), in line with the domain size obtained from in situ synchrotron XRD results[22].

At this stage, a mobile phase wets the Cu nanoparticles and forms a network between particles. This is shown in the highlighted area of Fig. 1k–o, where a bridge has formed between the top and bottom domains. This supports the attribution of those two domains as Cu and ZnO because of the known SMSI effect. This new mobile phase can be attributed to ZnO_x, as confirmed by in situ STEM–EELS measurements of similar bridge features, which showed a notable Zn contribution (Supplementary Fig. 7).

Upon cooling to 50 °C, we observe an increased coverage of ZnO_x on Cu surfaces, with varying morphologies. Particular care was taken to discriminate ZnO_x from possible carbon contamination, which is known to appear as shells of lower contrast over nanoparticles as

https://doi.org/10.1038/s41929-026-01514-x

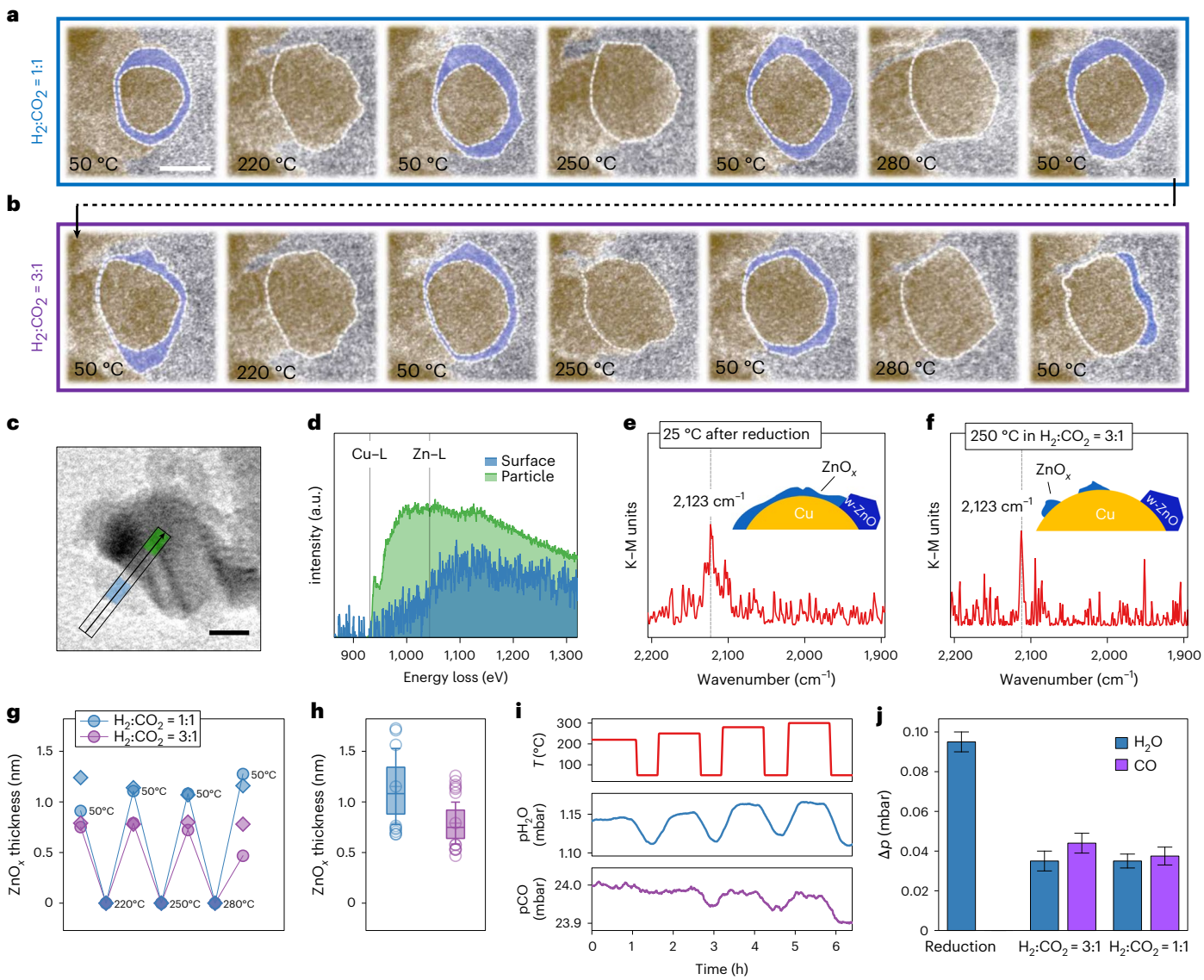

Fig. 3 | Impact of CO_2 content and temperature on the ZnO_x overlayer thickness. a,**b**, Evolution of a Cu nanoparticle as the temperature is switched between 50 °C and methanol synthesis temperatures (220–280 °C), for two different H_2:CO_2 ratios: 1:1 (**a**) and 3:1 (**b**). The boundaries of the Cu particle and the overlayer are highlighted by white dashes, and the overlayer coloured in blue. The dose rate was 1,105 e^- Å^{-2} s^{-1}. Scale bar, 5 nm. The original images are presented in Supplementary Fig. 16. **c**,**d**, In situ TEM observation (**c**) and in situ STEM–EELS analysis (**d**) of an island feature on a nanoparticle. In **d**, two spectra are integrated over the areas coloured in **c**. Scale bar, 5 nm. **e**,**f**, In situ DRIFTS measurements: at 50 °C after reductive activation at 250 °C and 1 bar (**e**); at 250 °C after 1 h in H_2:CO_2 = 3:1 at 1 bar (**f**). Heating rate: 5 K min^{-1}. K–M, Kubelka–Munk; w–ZnO denotes the wurtzite (w) polymorph of ZnO. **g**, Evolution of the average overlayer thickness at 50 °C in both feeds. Circles represent the particle of **a** and **b**, while diamonds represent the averages over all measurements on 12 particles during 1 operando experiment. In total, 81 measurements were collected: 43 for H_2:CO_2 = 1:1 and 38 for H_2:CO_2 = 3:1. There is no hysteresis between the successive heating and cooling cycles. **h**, Box plots of overlayer thickness measurements at 50 °C for the two gas compositions. Averages (crossed dots) are 1.1 ± 0.1 nm and 0.8 ± 0.1 nm for H_2:CO_2 = 1:1 and 3:1, respectively. The centre line is the median. The box top and bottom bounds are q3 and q1, respectively. The whiskers correspond to 1 standard deviation. **i**, Evolution of H_2O and CO partial pressures in a H_2:CO_2 = 1:1 feed. **j**, H_2O and CO partial pressure change from 50 to 250 °C. n = 1. The conditions in **a**, **c** and **d** are as follows: gas composition H_2:CO_2:He = 2:2:1, pressure 661 mbar, heating rate 10 K min^{-1}. The conditions in **b** and **i** are as follows: gas composition H_2:CO_2:He = 6:2:1, pressure 616 mbar, heating rate 10 K min^{-1}.

well, but does not disappear upon heating (Supplementary Fig. 8). Moreover, possible effects of the electron dose on ZnO_x were carefully considered and dismissed. Telltale signs of such irradiation damage are either the transition from graphitic ZnO_x to wurtzite[13], which forms faceted islands on Cu surfaces, or the progressive disappearance of the overlayer altogether (Supplementary Fig. 9 and 10 and Supplementary Videos 3–5). The reduced catalyst was stable when exposed to dose rates around 1,000 e^- Å^{-2} s^{-1} (Supplementary Video. 6). Both homogeneous shells and ZnO_x islands were found, with thicknesses ranging from 0.5 to 3 nm. This is reported in Supplementary Fig. 11, and indicates that the final composition of CZA catalysts is dynamic and that the density of favourable Cu–ZnO sites is not set by the synthesis or activation protocols, but evolves with the operating temperature of the catalyst.

In situ DRIFTS measurements at 25 °C after reduction at 250 °C ambient pressure (Fig. 3e) show a peak at 2,125 cm^{-1} that is characteristic of the adsorption of CO on graphitic ZnO_x (ref. 11). CO adsorption on metallic Cu was not observed, indicating full ZnO_x coverage. This is in agreement with previously published ex situ TEM and Raman results[13,20]. The former shows that a layer of 1–2 nm of graphitic ZnO_x surrounds the Cu nanoparticles at room temperature after reductive activation.

https://doi.org/10.1038/s41929-026-01514-x

Operation in CO_2 hydrogenation feeds

Next, the diluted hydrogen feed was evacuated and the reaction mixture H_2:CO_2:He = 2:2:1 was introduced. Imaging at 50 °C revealed clusters of nanoparticles exhibiting core–shell structures with overlayer thicknesses up to 2.4 nm (Fig. 3a). The temperature was then increased at a rate of 10 K min^{-1} to 220 °C, where it was maintained for 1 h, and the system was subsequently cooled to 50 °C for 30 min. This was repeated two more times for temperature plateaus at 250 °C and 280 °C, to study the effect of repeated heating and cooling cycles on the morphology of particle aggregates and the ZnO_x overlayer in particular (Fig. 3a). We find that the SMSI-induced ZnO_x overlayer systematically opens at reaction temperatures (Supplementary Fig. 12), leading to exposed Cu surfaces sparsely decorated with ZnO_x islands (Fig. 3c). These islands were further characterized by in situ STEM–EELS (Fig. 3d and Supplementary Fig. 7), corroborating the presence of Zn.

The ZnO_x overlayer reforms upon cooling with no significant hysteresis effect (Fig. 3g), to an average thickness of 1.1 ± 0.1 nm (Fig. 3h). Details of the overlayer segmentation procedure and raw TEM data can be found in Supplementary Figs. 13–16. This thickness is consistent with previous ex situ findings which reported 1–2 nm of ZnO_x surrounding the nanoparticles at ambient temperature[13]. Further sintering is also observed, with a population of particles disappearing into larger ones, most notably after the first plateau at 220 °C (Supplementary Fig. 17), in agreement with other in situ reports of sintering in operating conditions[22]. This is particularly noticeable in the highlighted particle of Fig. 3a, with the Cu core radius increasing from 3.1 nm after reduction and settling to a 4 ± 0.3 nm average in subsequent CO_2 hydrogenation heating and cooling cycles.

Following these cycles, the sample was allowed to cool down to 50 °C and the feed was exchanged to H_2:CO_2:He = 6:2:1 to investigate the influence of the feed composition on the SMSI. TEM results show that, although the ZnO_x overlayer has a similar temperature response as in the feed a larger CO_2 content (Fig. 3b), we observe the ZnO_x overlayer to be significantly thinner, at an average thickness of 0.8 ± 0.1 nm (Fig. 3h). This provides direct evidence that higher CO_2 contents promote the wetting of Cu surfaces by ZnO_x. Operando DRIFTS measurements recorded under reaction conditions (H_2:CO_2 = 3:1, 1 bar; Fig. 3f) at 250 °C showed a CO vibration at 2,112 cm^{-1}, which is shifted compared with vibrations expected for metallic Cu (2,093 cm^{-1})[11]. This indicates the existence of $Cu^{\delta+}$ surface species under reaction conditions, either at the perimeters of ZnO islands or due to subsurface oxygen, which is expected to form under reaction conditions[44,45]. The CO that probes these sites is itself the reaction product of CO_2 hydrogenation. Thus the catalyst is active throughout our measurement. Additional features below 2,100 cm^{-1} indicate the simultaneous presence of metallic Cu, consistent with an only partially decorated Cu surface seen in the images. The presence of a CuZn surface alloy in this hydrogen-rich feed cannot be excluded due to the tail of the peak towards lower wavenumbers.

It is important here to note that the discrepancy in ZnO_x coverage between the two CO_2 hydrogenation feeds used in this study was robust across multiple areas of the sample, across different experiments, and independent of whether a higher CO_2 content feed was used first or as the second step (Supplementary Fig. 18). Finally, we show that this phenomenon is associated with CO_2 hydrogenation catalysis, rather than only thermally driven. MS analysis reveals the presence of both H_2O and CO products, with rates that respond closely to the temperature profile (Fig. 3i). Further analysis shows that these products are present in a 1:1 ratio[46] (Fig. 3j), as would be expected from the RWGS reaction. This indicates that there is no excess water being produced from continuous reduction of ZnO, as this reaction is suppressed by CO_2 (ref. 47). Interestingly, the rate of CO production is the same across both feeds. This is in contrast with ex situ fixed-bed reactor results (Supplementary Fig. 19) which show that the CO_2 conversion is about

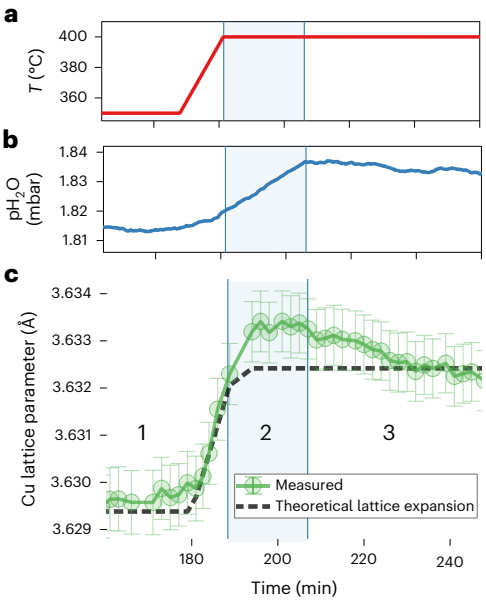

Fig. 4 | Evolution of the Cu lattice parameter at 400°C in H_2:CO_2 = 1:1 feed. **a**, Temperature profile. **b**, H_2O partial pressure. **c**, Measured Cu lattice parameter extracted from the Rietveld refinement of integrated SAED patterns (green markers) and predicted values from the theoretical thermal expansion of Cu. The errors bars correspond to Rietveld fitting errors. The conditions are as follows: gas composition H_2:CO_2:He = 2:2:1, pressure 661 mbar, heating rate 10 K min^{-1}, electron dose rate 3.4 e^- $Å^{-2}$ s^{-1}.

50% lower in the H_2:CO_2 = 1:1 feed than in the H_2:CO_2 = 3:1 feed. This discrepancy is probably related to the unconventional design of the gas cell nanoreactor, in which only a minuscule amount of the gas feed can interact with the few catalyst particles, causing an extremely high space velocity and a low conversion[46].

Role of H_2O in the re-oxidation of CuZn alloys

Last, we set out to investigate the transient nature of CuZn alloys in CZA catalysts as those species have been shown to be unstable under reaction conditions in previous reports[7,18,48]. To this end, the temperature was ramped up at a rate of 10 K min^{-1} to three plateaus at 300 °C, 350 °C and 400 °C. SAED patterns acquired every 2 min were processed to yield the Cu lattice parameter. These data are presented in Fig. 4 and Supplementary Fig. 20 alongside the predicted Cu lattice parameter from thermal expansion.

While the Cu lattice parameter evolves in excellent agreement with predictions from the thermal expansion up to 350 °C, it overshoots the thermal expansion baseline at 400 °C by 0.03% after 7.5 min. This is indicative of bulk CuZn alloy formation, which would be expected to proceed further as the 400 °C plateau is maintained. However, we observe a subsequent rapid drop in the Cu lattice parameter, which returns to a baseline over the next 25 min. This intriguing time response suggests a delayed re-oxidation of Zn species in the alloy, with the re-oxidation rate increasing throughout the 400 °C plateau. This may be explained by a delayed H_2O production after the temperature is quickly increased. Close analysis of the MS traces corresponding to H_2O reveals a time delay that matches the drop in the Cu lattice parameter (Supplementary Fig. 21). Moreover, H_2O is known to readily oxidize the Zn sites in CuZn alloys to form Cu–ZnO species[3,16]. This leads us to hypothesize the following sequence of events, as described in Fig. 4: initially, bulk CuZn alloying dominates as the temperature is raised from 350 °C to 400 °C. The Cu lattice parameter overshoots the expected thermal expansion baseline. Alloying kinetics are known to be slow because of the sluggish diffusion of Zn in Cu (1). Next, H_2O production rises in the nanoreactor. The Cu lattice

https://doi.org/10.1038/s41929-026-01514-x

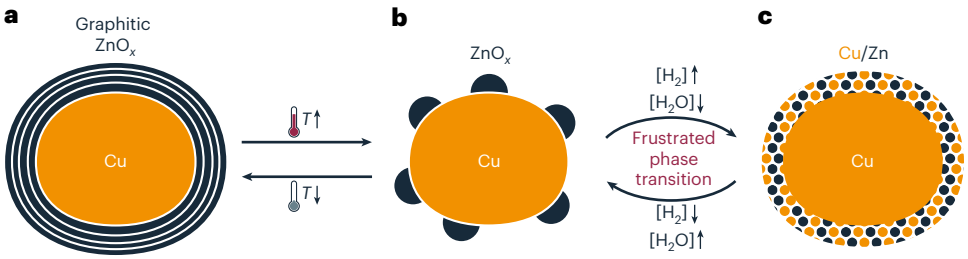

Fig. 5 | Proposed dynamics occurring in the Cu/ZnO system. a, At low temperatures, Cu nanoparticles are encapsulated by a graphitic ZnO_x shell. **b**,**c** When the temperature is increased, the overlayer opens and a Cu/ZnO_x perimeter is exposed to the reaction environment. The system then becomes active. We hypothesize that, between state (**b**) and the formation of CuZn surface alloys (**c**) a frustrated phase transition exists, which is mediated by changes of the local water and H_2 concentration under reaction conditions. At this point, which crucially depends on the reaction conditions and reflects the point of highest activity, the system is able to reversibly change between these two states. An arrow pointing upwards denotes an increase in temperature or concentration. An arrow pointing downwards denotes a decrease in temperature or concentration.

parameter temporarily stabilizes as the balance between alloying and re-oxidation rates shift towards the latter (2). Finally, H_2O production reaches its maximum rate approximately 16 min after the start of the temperature plateau (3). Re-oxidation overtakes CuZn alloying and the Cu lattice parameter returns to the baseline over the next 25 min. This behaviour was confirmed in a separate experiment, this time in the CO_2-rich feed H_2:CO_2:He = 2:2:1 (Supplementary Fig. 22). This further implies that the remarkable evolution of the Cu lattice parameter can be reproduced in a robust manner and demonstrates that coupling MS with electron diffraction data can yield unique insights into time-dependent phenomena.

Discussion

We report here an operando TEM investigation of an industrial relevant CZA catalyst that is known for its high methanol production rate[36]. Although there is an in situ TEM report that has focused on a similar system[25], to our knowledge there are no operando studies of such an industrial-like catalyst system at realistic operating temperatures. Our findings on the temperature-induced dynamics of the SMSI overlayer are also in line with recent operando TEM observations on Ni/TiO_2 model catalysts showing that the TiO_x overlayer opens at temperatures above 400 °C (ref. 31). We present direct evidence that the wetting of Cu surfaces by mobile partially reduced ZnO_x is reversible and depends on both the temperature and the amount of CO_2 in the feed.

It has been suggested that this phenomenon is mediated by the presence of surface CuZn alloy[5,9,12]. At lower temperatures, CO_2 and H_2O re-oxidize the surface Zn^0 species[7,22] to ZnO_x and thus promote the wetting of Cu surfaces by additional mobile ZnO_x species. When the temperature returns to CO_2 hydrogenation conditions, above 220 °C, CuZn alloy is formed on the surface of Cu particles and the wetting of Cu by ZnO_x becomes unfavourable[12]. In our second feed (H_2:CO_2 = 3:1), this may be compounded by the higher H_2 partial pressure, which fosters the formation of surface CuZn alloys[7,18,49,50], resulting in a thinner ZnO_x overlayer. These results show that the surface morphology of Cu nanoparticles, as well as the oxidation state of Zn, are highly dynamic during catalysis and do not depend solely on activation parameters, as previously suggested[7,18]. Cu surfaces are decorated by Zn^{2+} (ZnO_x islands) and Zn^0 atoms (CuZn alloy), in a manner dependent on the redox chemical potential of the gas phase[12]. Higher temperatures and more reductive conditions, such as higher CO (refs. 6,12) or H_2 partial pressures[7,18,20], can favour more CuZn alloy formation[7,20], while more oxidative conditions such as higher CO_2 (refs. 12,18) and H_2O partial pressures[6,7] can re-oxidize CuZn and yield a more extensive ZnO_x coverage and thus more Cu–ZnO interfacial sites at the perimeter of the ZnO islands[12]. Yet, an excessive CO_2 fraction in the feed will lead to a drop in the amount of available Cu–ZnO sites as the ZnO_x coverage becomes too high and blocks Cu surfaces[6].

Because CuZn alloys are rapidly re-oxidized[7,18,48], yet are nonetheless present under operating conditions[12], we propose that even at steady state, Zn^0 and ZnO_x species may coexist and continuously interconvert as local chemical potentials change throughout the catalytic cycle. It is crucial to control the reaction conditions that lead to the formation of these phases and trigger their interconversion. As both phases are catalytically active, it is not surprising that no easy distinction of the active phase seems possible[8].

The conditions associated with the highest catalytic performance could in fact correspond to a state of frustrated phase transition[51]. This is in line with previous results indicating that the re-oxidation of metallic Zn in the alloy can also yield zinc formate, a critical reaction intermediate[48]. This further implies that the continuous formation of CuZn alloy and its subsequent re-oxidation could be critical to the mechanism of CO_2 hydrogenation to methanol on CZA catalysts. Furthermore, if we extrapolate the CuZn alloying and re-oxidation behaviour shown here at 400 °C (Fig. 4) to more realistic operating conditions below 250 °C, it is reasonable to assume that for methanol synthesis the reaction product H_2O could contribute to a steady state where CuZn formation, re-oxidation of Zn in the alloy, and ZnO_x wetting of the Cu surfaces are happening concurrently. H_2O could contribute to create conditions in which the system is thermodynamically frustrated, partially oxidized and highly active, in line with the widely reported promotional effect of H_2O on methanol synthesis[52]. Moreover, we suggest that, as the catalyst ages, mobile Zn species crystallize as wurtzite ZnO domains[53] and do not contribute to this frustrated phase transition any longer, leading to deactivation (Fig. 5). This is in line with previous reports linking wurtzite ZnO on Cu nanoparticles surfaces to deactivation after 50 days on stream[5,53]. Thus, strategies to limit the loss of mobile Zn species, hinder irreversible ZnO crystallization and maintain the frustrated phase transition could result in improvements to the lifetime and activity of this catalyst system.

In summary, operando TEM was used to shed unique insight into the morphological and structural evolution of CZA catalysts during CO_2 hydrogenation. Coupling MS, electron diffraction and imaging yields a comprehensive description of the activation and reaction process. ZnO is seen to wet the surface of Cu nanoparticles upon reduction through the SMSI effect. Operando DRIFTS confirms that this is not merely a local observation, but rather one that applies to the entire catalyst. The catalyst morphology is overhauled upon cooling, with ZnO_x migrating further to Cu surfaces and resulting in an uneven coverage of either full overlayers or islands. Moreover, we show that the ZnO_x overlayer thickness depends on the CO_2 feed content, with higher CO_2 amounts associated with thicker overlayers. This sheds insight into how the chemical potential of the gas phase affects the balance of Zn^{2+} and Zn^0 species decorating Cu surfaces in operating conditions. The driving forces are the oxidizing potentials of H_2O and CO_2 and the reductive potentials

of H_2 and CO. This is correlated with the formation of RWGS products and, thus, catalytic operation as detected by online MS. Finally, we investigate the onset of bulk CuZn formation at higher temperatures. We observe a compelling evolution of the Cu lattice parameter over the 400 °C plateau, with an initial sharp temperature response that corresponds to CuZn alloying, and a delayed return to the Cu baseline as the H_2O level increases in the reactor. These results highlight the role of H_2O produced during CO_2 hydrogenation on the re-oxidation of Zn^0 species and demonstrate the potential of operando SAED combined with Rietveld refinement to investigate transient crystalline phases in metastable catalysts. Altogether, our results suggest that a frustrated phase transition between CuZn alloy and Cu–ZnO surface states could be key to the high performance of CZA catalysts for methanol synthesis. Understanding this system requires continued efforts with in situ and operando techniques into how the local chemical potential dynamically affects Zn redox chemistry on Cu surfaces.

Methods

Materials

The catalyst was synthetized following a protocol published previously[36,38] from the calcination of a zincian malachite precursor (ID S28807) with a Cu:Zn ratio of 70:30. The precursor was prepared by pH-controlled coprecipitation in an automated reactor (LabMax from Mettler-Toledo). The appropriate amount of $Zn(NO_3)_2{\cdot}6H_2O$ and $Cu(NO_3)_2{\cdot}3H_2O$ was dissolved in deionized water and 15 ml of concentrated HNO_3 to obtain 600 ml of a 1 M solution of the metal salts. This solution was added to the partially filled reactor at a constant rate of 20 ml min^{-1}. A Na_2CO_3 solution (1.6 M) was added automatically to keep the pH constant at 6.5. The precipitation temperature was adjusted to 338 K. This precipitation process was followed by an aging time of 1 h (338 K, pH 6.5) once the turbidity started to increase. The solid was then filter-collected and washed several times by redispersion in water until the conductivity of the washing medium was below 0.5 mS cm^{-1}. The solid hydroxycarbonate precursors were obtained by spray drying. Calcination of the precursor for 3 h at 603 K yielded the CuO–ZnO precatalysts (ID S29968).

Instruments

All experiments were performed in a Thermofisher/FEI Titan 80-300 operated at 300 kV and equipped with a TVIPS XF416 camera. An objective aperture of 40 µm was used to partially remove the amorphous SiN background and improve the contrast of TEM imaging. The amount of imaging was kept minimal by design, to limit electron irradiation of the sample. A strict low-dose imaging protocol was crucial to ensure that the total effective dose applied to areas of interest was only that of the acquired frames, with minimal excess to find and focus the specimen. A DENSsolutions Climate holder was used and connected to a homebuilt gas feeding system described in a previous publication[34].

Gas feed and temperature control

Gas mixtures were allowed to settle overnight to ensure a flat and stable MS baseline, which was critical to detect minute variation in trends. The MS column was baked for 48 h before the start of the experiment to desorb H_2O from the column walls and ensure a minimal H_2O base level. Three gas feeds were used: (1) diluted hydrogen, $He:H_2 = 9:1$, $pH_2 = 79$ mbar, (2) $H_2:CO_2:He = 2:2:1$, $pH_2 = 286$ mbar, $pCO_2 = 243$ mbar and (3) $H_2:CO_2:He=6:2:1$, $pH_2 = 482$ mbar, $pCO_2 = 89$ mbar. Gases were allowed to settle overnight after switching from one feed to another. The MS signal shows a rapid temperature response (<1 min) to temperature changes (Supplementary Fig. 20). This is important to the validity of the results reported Fig. 4. The delayed H_2O signal rise is not due to experimental reasons, but stems from the catalytic system itself.

TEM. Images were acquired with a dose rate of 1,105 e^- $Å^{-2}$ s^{-1} over 1 s, while SAED patterns used 3.4 e^- $Å^{-2}$ s^{-1} over 100 ms, averaging 100 frames. Temperature profiles used for reduction were adapted to enable TEM imaging at fixed temperatures. Two additional temperature plateaus of 15 min at 150 °C and 200 °C were incorporated to allow the TEM imaging of six areas of interest selected beforehand. SAED was acquired continuously every 30 s excluding imaging intervals. Particular care was also taken to discriminate ZnO_x from possible carbon contamination, which can also appear as low-contrast shells over nanoparticles but does not disappear upon heating (Supplementary Fig. 8). Moreover, possible effects of the electron dose on ZnO_x were carefully considered and dismissed. Telltale signs of such irradiation damage are either the transition from graphitic ZnO_x to wurtzite[13], which forms faceted islands on Cu surfaces, or the progressive disappearance of the overlayer altogether (Supplementary Fig. 9), possibly linked to an increased surface CuZn alloy formation as a result of the reducing effect of the electron beam. Both of these effects can be observed in the dataset reported Supplementary Fig. 10, which was acquired with a dose of about 3,000 e^- $Å^{-2}$ s^{-1}, a dose still below what is used in other recent in situ studies of this catalyst[6,24,25]. The reported radius of the nanoparticle and the values of the overlayer thickness are calculated from areas manually segmented on TEM images (Supplementary Fig. 13) assuming a spherical core–shell morphology. A flat area measurement error of ±5 nm^2 was used for the areas obtained by manual segmentation. This was used to estimate the errors in the reported thickness values. In total, 83 measurements were performed on 12 particles. The standard error of the mean was rounded up to 0.1 nm.

SAED analysis

SAED is particularly adapted to the study of beam-sensitive systems such as CZA catalysts, and particular attention was given to the analysis of SAED temperature series. For this, we combined subpixel accuracy centre finding and fourth-order astigmatism correction adapted from recently published methods[43], wavelet background removal[54] and Rietveld refinement for electron diffraction. The latter is done using MAUD, developed by Lutterotti et al.[42], which uses the Blackman two-beam approximation to correct for dynamic electron scattering. Published protocols were followed to determine the broadening function of our microscope using a reference sample of a single phase of monodisperse Cu_2O nanocubes that were well characterized by XRD. Rietveld fitting was performed with the following four phases for the reductive activation process in Fig. 2: Cu, CuO, Cu_2O and ZnO. Only Cu and ZnO were considered for the fully reduced catalyst in the dataset that went into Fig. 4. Graphitic-like ZnO_x can be ignored for SAED analysis owing to its negligible volume and absence at 250 °C as shown throughout the Article. The small particle size of our sample allows us to acquire perfect, isotropic ring patterns that can easily be fitted during the astigmatism correction step. Furthermore, the position of the Cu (111) and (200) reflections can be fitted easily as they are very sharp and their intensity is much larger than the background, especially after the dual wavelet background extraction.

DRIFTS. DRIFTS measurements were performed using an Agilent Cary 680 FTIR spectrometer equipped with a liquid-nitrogen-cooled MCT detector and a Harrick Praying Mantis diffuse reflectance accessory. The spectra were recorded with a spectral resolution of 2 cm^{-1} and 1,024 scan accumulations. Before the measurements, the optical path was aligned by minimizing the contribution of specular reflected light directed at the detector by using a mirror in the sample position. The calcined precursor (38.3 mg) was placed in an in situ cell (DRP) in combination with a high-temperature reaction chamber HVC-DRM-5 with a high-pressure dome with ZnSe windows, Harrick) and pretreated in 10% H_2 in Ar (flow rate 30.6 ml min^{-1}, heating rate 5 K min^{-1}, pressure 1 bar) for 2 h at 250 °C. After cooling down in pure Ar to 25 °C, a spectrum of the catalyst was recorded. CO adsorption was performed at 25 °C by adjusting an equilibrium pressure of 8 mbar CO (purity 3.7, Air Liquide). The spectrum was recorded using the single-beam spectrum of the

reduced catalyst at 25 °C as background to generate the spectrum of adsorbed CO. The operando experiment was performed using 36.9 mg of the calcined precursor and performing the same reduction procedure as described above. Then, the catalyst was heated in a gas mixture of CO_2:H_2:Ar = 1:3:1 (flow rate 29.5 ml min^{-1}, heating rate 10 K min^{-1}, pressure 1 bar) to 250 °C for 2 h and very short flushing with Ar at 250 °C. The single beam of the spectrum of the reduced catalyst recorded at 250 °C was used as background. The spectra of the adsorbed species were presented in Kubelka–Munk units $F(R_\infty) = (1 - R_\infty)^2/2\,R_\infty$.

Fixed-bed reactor testing

CO_2 hydrogenation reaction performance was tested at 1 bar with a fixed-bed reactor using a steel reactor tube with an inner diameter of 4 mm. The catalyst bed temperature was determined by correcting the temperature measured with a thermocouple located outside the tube. All products and unreacted educts were online analysed by a gas chromatograph (Agilent 7890) equipped with a thermal conductivity detector (permanent gas analysis) and a flame ionization detector (hydrocarbon analysis). The conversion factor of each gas was calculated with gas standards. The temperature between the reactor and the gas chromatograph was kept at 175 °C to avoid the condensation of the products. A 100-mg sample of the CZA catalyst was sieved into particles ranging in size from 100 µm to 200 µm and loaded into the reactor. Before the CO_2 hydrogenation testing, the catalyst was pretreated in 10 % H_2/Ar (80 ml min^{-1}) at 250 °C with a ramp rate of 4 °C min^{-1} and held for 2 h. After activation, the reactor was cooled to room temperature and heated to target temperature in the reaction feed. Two different reaction feeds were used: the ratios of CO_2/H_2/Ar were 20/20/60 and 20/60/20. The total flowing rate of two feeds kept at 80 ml min^{-1}. Ar was used as internal standard and for carbon balance calculation. For all testing, the deviation of the carbon balance from 100% was within 5%.

Data availability

Most raw data and excel files are available free of charge at https://ac.archive.fhi.mpg.de/D59869. Other data are available from the authors upon request.

Code availability

The Python routines (subpixel iterative centre finding, astigmatism correction, background removal and 1D integration) used to process the SAED data shown in this Article are available free of charge via GitHub at https://github.com/mboniboni/TEM_scripts. The centre finding and astigmatism correction algorithm are from Fritsch et al[43]. In addition, a Python implementation of MAUD—for the Rietveld fitting of processing SAED data—called MILK is available via GitHub at https://github.com/lanl/MILK (ref. 55).

References

1. Cui, X., Hou, D., Bing, Q., Hu, J. & Deng, D. Shaping the future of green methanol. *Chem Catal.* **5**, 101515 (2025).
2. Olah, G. A. Beyond oil and gas: the methanol economy. *Angew. Chem. Int. Ed.* **44**, 2636–2639 (2005).
3. Kattel, S., Ramírez, P. J., Chen, J. G., Rodriguez, J. A. & Liu, P. Active sites for CO_2 hydrogenation to methanol on Cu/ZnO catalysts. *Science* **355**, 1296–1299 (2017).
4. Nakamura, J., Choi, Y. & Fujitani, T. On the issue of the active site and the role of ZnO in Cu/ZnO methanol synthesis catalysts. *Top. Catal.* **22**, 277–285 (2003).
5. Laudenschleger, D., Ruland, H. & Muhler, M. Identifying the nature of the active sites in methanol synthesis over Cu/ZnO/Al_2O_3 catalysts. *Nat. Commun.* **11**, 3898 (2020).
6. Tu, W. et al. Gas-dependent active sites on Cu/ZnO clusters for CH_3OH synthesis. *J. Am. Chem. Soc.* **145**, 8751–8756 (2023).
7. Frei, E. et al. Cu–Zn alloy formation as unfavored state for efficient methanol catalysts. *ChemCatChem* **12**, 4029–4033 (2020).
8. Divins, N. J. et al. Operando high-pressure investigation of size-controlled CuZn catalysts for the methanol synthesis reaction. *Nat. Commun.* **12**, 1435 (2021).
9. Behrens, M. et al. The active site of methanol synthesis over Cu/ZnO/Al_2O_3 industrial catalysts. *Science* **336**, 893–897 (2012).
10. Studt, F. et al. The mechanism of CO and CO_2 hydrogenation to methanol over Cu-based catalysts. *ChemCatChem* **7**, 1105–1111 (2015).
11. Schumann, J., Kröhnert, J., Frei, E., Schlögl, R. & Trunschke, A. IR-spectroscopic study on the interface of Cu-based methanol synthesis catalysts: evidence for the formation of a ZnO overlayer. *Top. Catal.* **60**, 1735–1743 (2017).
12. Amann, P. et al. The state of zinc in methanol synthesis over a Zn/ZnO/Cu(211) model catalyst. *Science* **376**, 603–608 (2022).
13. Lunkenbein, T., Schumann, J., Behrens, M., Schlögl, R. & Willinger, M. G. Formation of a ZnO overlayer in industrial Cu/ZnO/Al_2O_3 catalysts induced by strong metal–support interactions. *Angew. Chem. Int. Ed.* **54**, 4544–4548 (2015).
14. Topsøe, H. Developments in operando studies and in situ characterization of heterogeneous catalysts. *J. Catal.* **216**, 155–164 (2003).
15. Kuld, S. et al. Quantifying the promotion of Cu catalysts by ZnO for methanol synthesis. *Science* **352**, 969–974 (2016).
16. Grunwaldt, J. D., Molenbroek, A. M., Topsøe, N. Y., Topsøe, H. & Clausen, B. S. In situ investigations of structural changes in Cu/ZnO catalysts. *J. Catal.* **194**, 452–460 (2000).
17. Frei, E. et al. Activating a Cu/ZnO: Al catalyst—much more than reduction: decomposition, self-doping and polymorphism. *ChemCatChem* **11**, 1587–1592 (2019).
18. Beck, A. et al. Following the structure of copper–zinc–alumina across the pressure gap in carbon dioxide hydrogenation. *Nat. Catal.* **4**, 488–497 (2021).
19. Kordus, D. et al. Shape-dependent CO_2 hydrogenation to methanol over Cu_2O nanocubes supported on ZnO. *J. Am. Chem. Soc.* **145**, 3016–3030 (2023).
20. Dalebout, R. et al. Insight into the nature of the ZnO_x promoter during methanol synthesis. *ACS Catal.* **12**, 6628–6639 (2022).
21. Gleißner, R. et al. Role of oxidation–reduction dynamics in the application of Cu/ZnO-based catalysts. *ACS Appl. Nano Mater.* **6**, 8004–8016 (2023).
22. Beck, A. et al. Drastic events and gradual change define the structure of an active copper–zinc–alumina catalyst for methanol synthesis. *Angew. Chem. Int. Ed.* **61**, e202200301 (2022).
23. Wagner, J. B. et al. In situ electron energy loss spectroscopy studies of gas-dependent metal–support interactions in Cu/ZnO catalysts. *J. Phys. Chem. B* **107**, 7753–7758 (2003).
24. Dong, Z., Liu, W., Zhang, L., Wang, S. & Luo, L. Structural evolution of Cu/ZnO catalysts during water–gas shift reaction: an in situ transmission electron microscopy study. *ACS Appl. Mater. Interfaces* **13**, 41707–41714 (2021).
25. Huang, X. et al. Visualizing structural and chemical transformations of an industrial Cu/ZnO/Al_2O_3 pre-catalyst during activation and CO_2 reduction. *ChemCatChem* **14**, e202201280 (2022).
26. Plodinec, M., Nerl, H. C., Girgsdies, F., Schlögl, R. & Lunkenbein, T. Insights into chemical dynamics and their impact on the reactivity of Pt nanoparticles during CO oxidation by operando TEM. *ACS Catal.* **10**, 3183–3193 (2020).
27. Chee, S. W., Arce-Ramos, J. M., Li, W., Genest, A. & Mirsaidov, U. Structural changes in noble metal nanoparticles during CO oxidation and their impact on catalyst activity. *Nat. Commun.* **11**, 1–9 (2020).
28. Vendelbo, S. B. et al. Visualization of oscillatory behaviour of Pt nanoparticles catalysing CO oxidation. *Nat. Mater.* **13**, 884–890 (2014).

29. Beck, A., Huang, X., Artiglia, L., Zabilskiy, M. & Wang, X. The dynamics of overlayer formation on catalyst nanoparticles and strong metal-support interaction. *Nat. Commun.* **11**, 3220 (2020).
30. Zhang, S. et al. Dynamical observation and detailed description of catalysts under strong metal-support interaction. *Nano Lett.* **16**, 4528–4534 (2016).
31. Monai, M. et al. Restructuring of titanium oxide overlayers over nickel nanoparticles during catalysis. *Science* **380**, 644–651 (2023).
32. De Smit, E. et al. Nanoscale chemical imaging of a working catalyst by scanning transmission X-ray microscopy. *Nature* **456**, 222–225 (2008).
33. Creemer, J. F. et al. Atomic-scale electron microscopy at ambient pressure. *Ultramicroscopy* **108**, 993–998 (2008).
34. Plodinec, M. et al. Versatile homebuilt gas feed and analysis system for operando TEM of catalysts at work. *Microsc. Microanal.* **26**, 220–228 (2020).
35. Beck, A., Newton, M. A., van de Water, L. G. A. & van Bokhoven, J. A. The enigma of methanol synthesis by $Cu/ZnO/Al_2O_3$-based catalysts. *Chem. Rev.* **124**, 4543–4678 (2024).
36. Schumann, J. et al. Synthesis and characterisation of a highly active Cu/ZnO:Al catalyst. *ChemCatChem* **6**, 2889–2897 (2014).
37. Galván, C. et al. Reverse water–gas shift reaction at the Cu/ZnO interface: influence of the Cu/Zn ratio on structure–activity correlations. *Appl. Catal. B* **195**, 104–111 (2016).
38. Schumann, J., Tarasov, A., Thomas, N., Schlögl, R. & Behrens, M. Cu,Zn-based catalysts for methanol synthesis: on the effect of calcination conditions and the part of residual carbonates. *Appl. Catal. A* **516**, 117–126 (2016).
39. Tarasov, A., Schumann, J., Girgsdies, F., Thomas, N. & Behrens, M. Thermokinetic investigation of binary Cu/Zn hydroxycarbonates as precursors for Cu/ZnO catalysts. *Thermochim. Acta* **591**, 1–9 (2014).
40. Živković, A., Solsona-Delgado, V., van der Linden, B., de Leeuw, N. H. & Melián-Cabrera, I. Molecular-level understanding of interfacial carbonates in stabilizing $CuO–ZnO(Al_2O_3)$ catalysts. *J. Catal.* **425**, 406–421 (2023).
41. Kurr, P. et al. Microstructural characterization of $Cu/ZnO/Al_2O_3$ catalysts for methanol steam reforming—a comparative study. *Appl. Catal. A* **348**, 153–164 (2008).
42. Sinha, A., Bortolotti, M., Ischia, G., Lutterotti, L. & Gialanella, S. Electron diffraction characterization of nanocrystalline materials using a Rietveld-based approach. Part I. Methodology. *J. Appl. Crystallogr.* **55**, 953–965 (2022).
43. Fritsch, B. et al. Sub-Kelvin thermometry for evaluating the local temperature stability within in situ TEM gas cells. *Ultramicroscopy* **235**, 113494 (2022).
44. Pacchioni, G. From CO_2 to methanol on $Cu/ZnO/Al_2O_3$ industrial catalyst. What do we know about the active phase and the reaction mechanism?. *ACS Catal.* **14**, 2730–2745 (2024).
45. Schlögl, R. Chemical batteries with CO_2. *Angew. Chem. Int. Ed.* **61**, e202007397 (2022).
46. Chee, S. W., Lunkenbein, T., Schlögl, R. & Cuenya, B. R. In situ and operando electron microscopy in heterogeneous catalysis—insights into multi-scale chemical dynamics. *J. Phys. Condens. Matter* **33**, 153001 (2021).
47. King, D. S. & Nix, R. M. Thermal stability and reducibility of ZnO and Cu/ZnO catalysts. *J. Catal.* **160**, 76–83 (1996).
48. Zabilskiy, M. et al. The unique interplay between copper and zinc during catalytic carbon dioxide hydrogenation to methanol. *Nat. Commun.* **11**, 2409 (2020).
49. Kuld, S., Conradsen, C., Moses, P. G., Chorkendorff, I. & Sehested, J. Quantification of zinc atoms in a surface alloy on copper in an industrial-type methanol synthesis catalyst. *Angew. Chem. Int. Ed.* **53**, 5941–5945 (2014).
50. Holse, C. et al. Dynamic behavior of CuZn nanoparticles under oxidizing and reducing conditions. *J. Phys. Chem. C* **119**, 2804–2812 (2015).
51. Cao, J. et al. In situ observation of oscillatory redox dynamics of copper. *Nat. Commun.* **11**, 3554 (2020).
52. Sahibzada, M., Metcalfe, I. S. & Chadwick, D. Methanol synthesis from $CO/CO_2/H_2$ over $Cu/ZnO/Al_2O_3$ at differential and finite conversions. *J. Catal.* **174**, 111–118 (1998).
53. Lunkenbein, T. et al. Bridging the time gap: a copper/zinc oxide/aluminum oxide catalyst for methanol synthesis studied under industrially relevant conditions and time scales. *Angew. Chem. Int. Ed.* **55**, 12708–12712 (2016).
54. René de Cotret, L. P., Otto, M. R., Stern, M. J. & Siwick, B. J. An open-source software ecosystem for the interactive exploration of ultrafast electron scattering data. *Adv. Struct. Chem. Imaging* **4**, 11 (2018).
55. Savage, D. J. et al. MILK: a Python scripting interface to MAUD for automation of Rietveld analysis. *J. Appl. Crystallogr.* **56**, 1277–1286 (2023).

Acknowledgements

We acknowledge the Federal Ministry of Education and Research of Germany (Bundesministerium für Bildung und Forschung, BMBF) in the framework of the CatLab project (03EW0015B) as well as Carbon2Chem (03EK3039D) for funding. T.L. also thanks the Deutsche Forschungsgemeinschaft (DFG, German Research Foundation) under Germany's Excellence Strategy-EXC2089/1- 390776260.

Author contributions

T.L. and M.B. conceived the project. M.B. performed TEM measurements and designed the SAED acquisition and analysis protocols together with T.G. E.F. synthesized the catalyst. J.D. and A.T. carried out fixed-bed reactor catalysis measurements. J.K. carried out the DRIFTS measurements. M.B. wrote the original manuscript. All authors discussed and commented on the manuscript.

Funding

Open access funding provided by Max Planck Society.

Competing interests

The authors declare no competing interests.

Additional information

Supplementary information The online version contains supplementary material available at https://doi.org/10.1038/s41929-026-01514-x.

Correspondence and requests for materials should be addressed to Maxime Boniface or Thomas Lunkenbein.

Peer review information *Nature Catalysis* thanks Langli Luo, Jakob B. Wagner and the other, anonymous, reviewer(s) for their contribution to the peer review of this work.